Challenges of sulfur SAD phasing as a routine method in macromolecular crystallography

James Doutch,‡ Michael A. Hough,¶ S. Samar Hasnain* and Richard W. Strange*

Molecular Biophysics Group, Barkla X-ray Laboratory of Biophysics, Faculty of Health and Life Sciences, University of Liverpool, Liverpool L69 7ZB, UK. E-mail: s.s.hasnain@liverpool.ac.uk, r.strange@liverpool.ac.uk

The sulfur SAD phasing method allows the determination of protein structures *de novo* without reference to derivatives such as Se-methionine. The feasibility for routine automated sulfur SAD phasing using a number of current protein crystallography beamlines at several synchrotrons was examined using crystals of trimeric *Achromobacter cycloclastes* nitrite reductase (*Ac*NiR), which contains a near average proportion of sulfur-containing residues and two Cu atoms per subunit. Experiments using X-ray wavelengths in the range 1.9–2.4 Å show that we are not yet at the level where sulfur SAD is routinely successful for *automated* structure solution and model building using existing beamlines and current software tools. On the other hand, experiments using the shortest X-ray wavelengths available on existing beamlines could be routinely exploited to solve and produce unbiased structural models using the similarly weak anomalous scattering signals from the intrinsic metal atoms in proteins. The comparison of long-wavelength phasing (the Bijvoet ratio for nine S atoms and two Cu atoms is $\sim$1.25% at $\sim$2 Å) and copper phasing (the Bijvoet ratio for two Cu atoms is 0.81% at $\sim$0.75 Å) for *Ac*NiR suggests that lower data multiplicity than is currently required for success should in general be possible for sulfur phasing if appropriate improvements to beamlines and data collection strategies can be implemented.

1. Introduction

Ten years ago, in the light of the high-throughput structural genomics initiatives being planned worldwide, it was thought that single-wavelength anomalous diffraction (SAD) phasing, using sulfur (S-SAD), intrinsic metal atoms or Se-methionine (Se-Met), would become a standard method of automated structure determination on synchrotron beamlines (*e.g.* Weiss *et al.*, 2001). This is now very much the case for Se-Met; however, the potential of native sulfur phasing has not yet been fulfilled on a similar scale. The obvious success of Se-Met experiments is clearly a factor. By replacing several weak S anomalous scatterers in a protein by several strong Se anomalous scatterers, and with the added option of wavelength optimization, not possible with S due to the absorption edge being at much longer wavelengths ($\sim$5 Å, 2.47 keV), there is almost a guarantee of the experiment successfully yielding a final structure. This focus on experiments conducted

at the Se K-edge (0.98 Å, 12.6 keV) means that the majority of current protein crystallography beamlines are designed to operate optimally around this energy.

A key advantage of the S-SAD phasing method in protein crystallography is the ability to obtain *de novo* crystal structures from native proteins, avoiding problems associated with non-isomorphism or the need to grow selenomethionine substitutes (Dauter *et al.*, 1999). As the vast majority of proteins contain either methionine and/or cysteine residues, the method has a huge potential (Ramagopal *et al.*, 2003) and in principle S-SAD should be a routine matter for a crystallographer using a synchrotron beamline with access to suitable X-ray wavelengths (Weiss, Sicker, Djinovic Carugo *et al.*, 2001). In practice, the available wavelengths are significantly shorter than the 'optimal' sulfur K-absorption edge (5.02 Å) where major technical challenges arise in the design and operation of beamlines (Behrens *et al.*, 1998; Stuhrmann *et al.*, 1997). Further difficulties arise due to the requirement for the end-station to be in a vacuum or low-pressure environment with all the consequent complications of remote sample handling. Only a small number of beamlines have been specifically designed to offer functionality at wavelengths

---

 19

greater than 3 Å ['long wavelengths' (Djinović Carugo et al., 2005)] for structural biology; for example, A1 at HASYLAB, Hamburg, Germany (Stuhrmann et al., 1997), and beamline ID01, ESRF, Grenoble, France (Boesecke et al., 2009; Carpentier et al., 2002), which allows direct access to the sulfur absorption edge. Their utilization as general facilities for S-SAD has remained limited. More typically, X-ray wavelengths in the 1.5–2.5 Å range on 'standard' synchrotron beamlines have been used for S-SAD experiments (Liu et al., 2000; Ramagopal et al., 2003; Cianci et al., 2008; Wang et al., 2006; Liu et al., 2000) as well as providing a significant anomalous signal for other heavy atoms, like Ca, Cl and P (Mueller-Dieckmann et al., 2007).

Both copper and chromium anodes (wavelengths 1.54 Å and 2.29 Å) have been increasingly employed for the same purpose in laboratory X-ray sources with success (Lemke et al., 2002; Debreczeni et al., 2003; Yang et al., 2003; Watanabe et al., 2005; Sarma & Karplus, 2006; Nan et al., 2009). While the view has gained ground over the past decade that S-SAD experiments should be routinely possible on existing ('longer wavelengths', 1.5–3 Å) X-ray beamlines (Weiss, Sicker, Djinovic Carugo et al., 2001; Djinović Carugo et al., 2005), it does not follow that these experiments are routinely successful, in that they nearly always lead to complete structures or even interpretable electron density maps. If the S-SAD method were truly routine, the number of beam time applications and the outcome of each synchrotron visit should be comparable with the success rate now seen for Se-SAD experiments, where new structures are reported on a regular basis, and where the path from initial data to final model is highly automated for well diffracting crystals.

Compared with the success of Se-Met methods, S-SAD is regarded as a more 'hit and miss' affair, largely due to the very weak S anomalous signal found at the energies typically accessible at 'standard' macromolecular crystallography (MX) beamlines. Since highly redundant diffraction data are needed for accurate measurement of this weak signal, a conflict arises between the desire to collect highly redundant data and consequent dose-dependent radiation damage. This damage can thwart structure solution efforts, either through global effects on crystal order and diffraction power or more specifically by causing structural changes in the vicinity of the anomalous scatterers (González et al., 2005; Ravelli et al., 2005; Ravelli & Garman, 2006). Many of the perceived difficulties are gradually being overcome by modern synchrotron beamline technologies and data collection strategies that aim to allow high multiplicity data with 'maximum useful data' for minimum X-ray dose alongside increasingly sophisticated software tools (e.g. accurate scaling of small anomalous differences, semi-automated model building into low-resolution electron density maps). Modern X-ray detectors such as Pilatus (Heinrich et al., 2009) are contributing to the aim of achieving greater redundancy for a given absorbed dose, while several dedicated beamlines are under construction for S-SAD. It has recently been argued that data accuracy at the low resolutions typically associated with longer-wavelength phasing experiments is limited by experimental factors and

that high multiplicity is only required because of systematic errors owing to instrumentation (Diederichs, 2010). Here, a systematic study is performed to explore just how capable standard MX beamlines, combined with the latest software tools, are at accomplishing S-SAD structure solution and producing protein models in a routine, largely automated, manner. Our results have direct implications both for existing crystallographic beamlines and the dedicated long-wavelength beamlines under construction/development.

2. Materials and methods

2.1. Crystallization

AcNiR was isolated from cells of Achromobacter cycloclastes as previously described (Antonyuk et al., 2005). Crystals were grown using the vapour-diffusion hanging-drop method, with a protein concentration of 20–30 mg ml^{-1} and reservoir solution of 1.1–1.6 M ammonium sulfate and 0.1 M sodium acetate, pH 4.75; crystallization was initiated by seeding. The crystals harvested for the experiments were of varying sizes, ranging between 0.05 and 0.6 mm per edge, and were soaked in 3.5 M sodium malonate pH 5.0 as a cryoprotectant solution before flash-cooling either by plunging into liquid nitrogen or by transfer to a 100 K cryostream prior to data collection. Crystals were mounted on short cryo-loops to minimize possible loop vibrations in the cryostream during data collection (Alkire et al., 2008).

2.2. Data collection and processing

Data were collected from protein crystallography in vacuum undulator beamlines I02 and I03 at the Diamond Light Source (DLS; Oxford, UK), PROXIMA I at SOLEIL (Gif-sur-Yvette, France), both using ADSC Q315 3×3 CCD detectors, X06SA and X10SA at the Swiss Light Source (SLS; Zurich, Switzerland) using a Pilatus 6M detector, 22-ID at the Advanced Photon Source (APS; Chicago, USA) using a MAR300 CCD detector, and the multipole wiggler MAD beamline 10 at the Daresbury Synchrotron Radiation Source (SRS; Warrington, UK) using a MARMosaic 225 CCD detector. For S-SAD experiments, crystals of dimensions <0.2 mm and wavelengths between 1.9 and 2.4 Å were used. 'Native' high-resolution datasets were recorded using larger crystals at a wavelength of 0.98 Å for use in phase-extension and model building, and the shortest available wavelengths (0.7–0.8 Å) were used for phasing experiments using the intrinsic Cu atoms present in AcNiR. Fifteen sequential datasets were also measured at SLS from a single AcNiR crystal using an X-ray wavelength of 0.75 Å, and the phasing power for a total accumulated dose of up to 6.9 MGy examined. Absorbed X-ray doses were estimated using the program RADDOSE (Paithankar et al., 2009). The beam was attenuated in all experiments by up to 95% in order to minimize radiation damage effects. Experiments were carried out at each beamline using randomly oriented crystals. Alternative strategies that may help to limit systematic errors associated with X-ray absorption or radiation damage, such as inverse-

beam data collection or the use of kappa geometry, were not used in the present study. Images from DLS, SOLEIL and the SRS were indexed and integrated using *Mosflm* (Leslie, 1992) and then merged and scaled in *SCALA* (Evans, 2006); the Pilatus images from the SLS were processed using *XDS* (Kabsch, 2010) and then *SCALA*. The scaling option in *SCALA* for secondary beam absorption corrections provided the largest anomalous signal for the long-wavelength datasets, as represented by $R_{anom}/R_{p.i.m}$ (Weiss, 2001). The APS data were processed using *HKL2000* (Otwinowski & Minor, 1997).

2.3. Heavy-atom phasing and structure solution

The *SHELX* program suite (Sheldrick, 2008) was used to analyse the heavy-atom substructure of each dataset (*SHELXC*), find the positions of the anomalous scatterers (*SHELXD*) and obtain the initial phase information (*SHELXE*). Approximately 1000 trial runs of *SHELXD* (Schneider & Sheldrick, 2002) were performed to find heavy-atom positions, with 20 to 50 cycles of phase refinement in *SHELXE* (Sheldrick, 2002). Extending the resolution beyond the experimental resolution [the 'free lunch algorithm' (Usón *et al.*, 2007)] may have been beneficial for subsequent model building but was not used here. Subsequent density modification was achieved using the program *DM* (Cowtan, 1994). The final phases obtained by this procedure were then used by the automated model-building routines in *ARP/wARP7.1* (Langer *et al.*, 2008; Morris *et al.*, 2003; Perrakis *et al.*, 1999) to construct an atomic model, which was refined using *REFMAC5* (Murshudov *et al.*, 1997) in the *CCP4i* program suite (Collaborative Computational Project, Number 4, 1994). Heavy-atom solution, phasing, refinement and model building of low-resolution datasets were also carried out using the *PHENIX* suite (Adams *et al.*, 2010). Electron density maps were viewed using *COOT* (Emsley & Cowtan, 2004). Where SAD phasing or model building failed, the atomic resolution structure of resting state *Ac*NiR (Antonyuk *et al.*, 2005) was used as the starting point for refinement so as to allow analysis of the factors (*e.g.* shifts in heavy-atom positions, *B*-factors) contributing to the lack of phasing success.

3. Results

This study provides a snapshot of the capabilities of several modern variable-wavelength protein crystallography beamlines for performing S-SAD experiments using the longest accessible wavelengths, in practice covering the wavelength range 1.9–2.4 Å. Experiments have been performed on beamlines I02 and I03 at the DLS, X06SA and X10SA at the SLS, Proxima-I at SOLEIL, BL10 at the SRS, and 22-ID at the APS. These are all operational beamlines, with the exception of BL10, which ceased operating in August 2008 with the closure of the SRS at Daresbury. No special arrangements or alterations to any of the beamlines or their equipment were made; they were used 'as available to users' during standard visits to the respective synchrotrons. Recognized software available on protein crystallography beamlines worldwide,

Table 1
Anomalous scattering coefficient f'' for Cu and S in the wavelength range 0.75–2.4 Å.

Wavelength (Å)	f''(S)	f''(Cu)
1.9	0.83	0.87
2.4	1.26	1.31
0.75	0.14	1.39

including *Mosflm* (Leslie, 1992), the *SHELX* suite (Sheldrick, 2002, 2008), the *PHENIX* suite (Adams *et al.*, 2002, 2010; Terwilliger, 2004; Terwilliger *et al.*, 2008), *REFMAC* (Murshudov *et al.*, 1997; Mooij *et al.*, 2009) and *ARP/wARP* (Langer *et al.*, 2008; Morris *et al.*, 2003; Perrakis *et al.*, 1999), were used for data processing, analysis, model building and refinement. The current software tools for *ab initio* phasing and model building from experimental electron density maps increasingly allow complete crystallographic models to be constructed with minimal manual intervention. For the purposes of this work, therefore, 'phasing and structure solution' were considered successful if it was possible to automatically build more than 90% of a protein model from the data and initial electron density maps using *PHENIX* or *ARP/wARP*.

The trimeric copper-containing nitrite reductase from *Achromobacter cycloclastes* (*Ac*NiR) was used as a model system for these experiments. The structures of native and ligand-bound *Ac*NiRs have been solved to better than 1 Å resolution (Antonyuk *et al.*, 2005). The cubic symmetry ($P2_13$) of the *Ac*NiR crystals was advantageous for rapidly collecting high-multiplicity data while minimizing the X-ray dose. The average eukaryotic protein contains around four S atoms for every 100 residues (Ramagopal *et al.*, 2003). *Ac*NiR has only 2.9% sulfur-containing residues and is somewhat more representative than the systems that have been typically used for S phasing at long wavelengths (Mueller-Dieckmann *et al.*, 2005, 2007). For example, lysozyme has ten sulfur atoms in 129 residues while insulin has six sulfur atoms in 51 residues (Cianci *et al.*, 2008; Debreczeni *et al.*, 2003; Yang *et al.*, 2003; Watanabe *et al.*, 2005). A single 37 kD subunit of *Ac*NiR has 340 amino acids, including nine methionines and one cysteine residue. Methionine 340, the final residue at the C-terminus, is more disordered than the others. Two Cu atoms are also present per subunit that contribute a comparable anomalous signal to S in the wavelength range used (Table 1). The anomalous signal estimated by the Bijvoet amplitude ratio ($\langle \Delta F^{\pm}/F \rangle$) at zero diffraction angle (Hendrickson & Teeter, 1981) for these 11 anomalous scatterers is 1.15–1.75% in the X-ray range 1.9–2.4 Å. The lower Bijvoet value is about twice[1] the Wang limit (Wang *et al.*, 2006). Thus, we would anticipate that extracting experimental S-SAD phase information from

---

[1] How close to the Wang limit is it possible to go for a successful experiment is a moot point. Using the same APS beamline that we used for S-SAD experiments (described below) that were beset with problems of harmonic contamination (at the time) at wavelengths above 1.8 Å, Dauter and colleagues were able to solve the structure of proteinase K, containing ten S, one Cl and one Ca atoms, using 0.98 Å X-rays with an expected Bijvoet ratio of only 0.46% (Wang *et al.*, 2006).

Table 2
Crystallographic data collection and processing statistics for crystals of *A. cycloclastes* nitrite reductase measured at different synchrotron beamlines.

The resolution cut-off for each dataset is determined by the wavelength and beamline geometry. The data are >99% complete overall and in the highest-resolution shells. The overall and highest-resolution (outer) shell statistics are shown for $I/\sigma(I)$, R_{meas}, $R_{p.i.m}$ and R_{anom}, where $R_{meas} = \sum_{hkl}[N/(N-1)]^{1/2} \times \sum_i |I_i(hkl) - \langle I(hkl)\rangle| / \sum_{hkl}\sum_i I_i(hkl)$, $R_{p.i.m} = \sum_{hkl}[1/(N-1)]^{1/2}\sum_i |I_i(hkl) - \langle I(hkl)\rangle| / \sum_{hkl}\sum_i I_i(hkl)$, $R_{anom} = [\sum_{hkl}|I^+(hkl) - I^-(hkl)|] / \sum_{hkl} I(hkl)$. R-factors show (all shells)/(outer shell); d''/σ is the anomalous signal indicator provided by *SHELXC*. The values quoted are from the high-resolution limit to 8 Å resolution for each dataset, with a value of about 0.8 indicating zero signal (Sheldrick, 2008).

SR source	Beamline	λ (Å)	Rotation (°)	Observations/ unique	Resolution (Å)	R_{meas} (%)	$R_{p.i.m.}$ (%)	R_{anom} (%)	$I/\sigma(I)$	Multiplicity/ anomalous	d''/σ	$R_{anom}/R_{p.i.m.}$
DLS	I03	2.40	720	668298/8737	56.0–2.69	7.7/13.3	1.1/2.3	3.2/8.4	70/41	77/40	1.36–3.38	2.9/3.7
			First 360	334005/8729		7.5/11.6	1.3/2.8	2.3/7.2	55/34	38/20	1.04–2.74	1.7/2.6
			Last 360	342230/8737		7.2/12.0	1.2/2.2	1.7/4.5	55/32	39/21	0.99–2.73	1.4/2.0
SOLEIL	Proxima I	2.07	360	473702/15912	47.5–2.20	6.7/9.7	1.1/3.1	1.5/4.2	49/18	32/16	0.64–1.84	1.4/1.4
SLS	X06SA	2.00	720	852147/13057	47.6–2.30	7.4/10.9	0.9/1.9	1.3/2.4	66/34	65/34	0.99–1.76	1.4/1.3
			First 360	425292/13057		7.2/10.3	1.2/2.5	1.4/2.8	48/25	33/17	0.84–1.27	1.2/1.1
			Last 360	426849/13057		7.3/11.2	1.2/2.7	1.4/2.9	47/24	33/17	0.83–1.24	1.2/1.1
APS	ID22	1.90	360	579156/14321	68.0–2.24	5.3/12.5	–	–	92/33	40	0.83–2.14	–
SRS	BL10	2.07	360†	763511/21055	54.9–1.96	13.3/50.3	2.2/8.6	1.9/7.6	29/11	37/19	0.89–1.29	0.9/0.9
	Crystal 1		120	283094/20868	30.1–1.96	8.4/50.2	2.3/14.3	2.5/13.0	25/7	14/7		1.1/0.9
	Crystal 2		120‡	196828/20318	47.7–1.96	5.8/63.4	1.8/19.6	2.4/24.2	23/4	10/5		1.3/1.2
	Crystal 3		120	282399/20863	54.9–1.96	6.6/24.2	1.8/6.8	2.1/6.8	31/13	14/7		1.2/1.0
Cu phasing												
SLS	X06SA	0.75	360	2444687/79404	42.5–1.25	6.9/18.4	1.8/4.6	1.3/3.3	40/21	31/16	0.76–0.80	0.7/0.7
			90	577445/79269		6.9/17.9	2.6/6.5	2.8/7.3	19/10	7/4	0.74–0.76	1.1/1.1
			90	99517/14815	42.5–2.20	4.5/6.0	1.8/2.2	2.0/2.5	35/32	7/3		1.1/1.1

† Dataset comprising crystal 1 + 2 + 3 scaled and merged.   ‡ Dataset is 97% complete.

*Ac*NiR crystals should be feasible for any of the current beamlines capable of tuning to these wavelengths. Attention is also given to the capabilities for Cu-SAD phasing using the shortest wavelengths (<1 Å) available at the same beamlines.

3.1. Phasing using S-SAD

Overall, S-SAD structure solution and auto-model building to final models succeeded in just over 60% of the datasets recorded from the *Ac*NiR crystals. Selected examples from successful cases for each of the beamlines/synchrotrons used are described below and are summarized in Table 2.

The approach followed was to collect diffraction data over a total crystal rotation range of 720° with an exposure time of 1 s per 1° oscillation, with the exception of data measured at X06SA, where each 1° oscillation used an exposure time of 0.15 s, to give a final redundancy (multiplicity) of ∼80. *SHELXD* was used to find the sites of the nine S atoms using this dataset and for a sub-set of the data, consisting of either the first or the last 360° collected (redundancy ≃ 40) (Table 2). The electron density maps subsequently produced by *SHELXE* and modified by *DM* (Cowtan, 1994) were then used for automated model building in *ARP/wARP*. If the resulting model was incomplete, two approaches were tried with the aim of improving the structural model using software. In the first, the initial phase information obtained by *SHELXE* was extended to higher resolution by using the low-resolution phase information with the amplitudes of the 0.98 Å wavelength 'native' dataset. The second approach used the *PHENIX* suite to build a model at lower resolution from

the initial long-wavelength dataset, either using the S atom solutions from *SHELXD* or using the heavy-atom solutions provided by the *HySS PHENIX* routine (Grosse-Kunstleve & Adams, 2003), with *PHASER* (McCoy *et al.*, 2007) used to provide initial phases. In these and subsequent cases reported, the residues that were not built are largely located at the N- and C-terminal ends of the amino acid sequence and in the bend containing the isolated β-bridge between residues 190 and 202 (making a gap between the two largest fragments).

3.1.1. Experiments at SLS and SOLEIL. At SLS beamline X06SA diffraction data were recorded at a wavelength of 2 Å and collected to a maximum resolution of 2.3 Å. *SHELXD* found the correct position for nine S atoms in 32 out of 1000 trials. Automatic model building with *ARP/wARP* or *PHENIX* failed at 2.3 Å resolution, while four fragments comprising 244 residues could be modelled automatically by *PHENIX* using the phases extended to 2 Å. The structure was successfully traced by *ARP/wARP* when combined with a native dataset to 1.4 Å resolution, when two amino acid chain fragments comprising 328 of the 340 residues were automatically fitted into the electron density map.

Using the standard beamline geometry on PROXIMA-I at SOLEIL, the longest wavelength available was 2.25 Å with a maximum data resolution of 3.1 Å. The S atom positions could not be located from a dataset recorded under these conditions in more than 5000 trials of *SHELXD*, nor was *PHENIX* successful. More was achieved using a wavelength of 2.07 Å, which allowed data to be collected to 2.2 Å resolution, resulting in a solution using 360 1° oscillation images (Table 2). *PHENIX* was able to build a model consisting of 290 residues
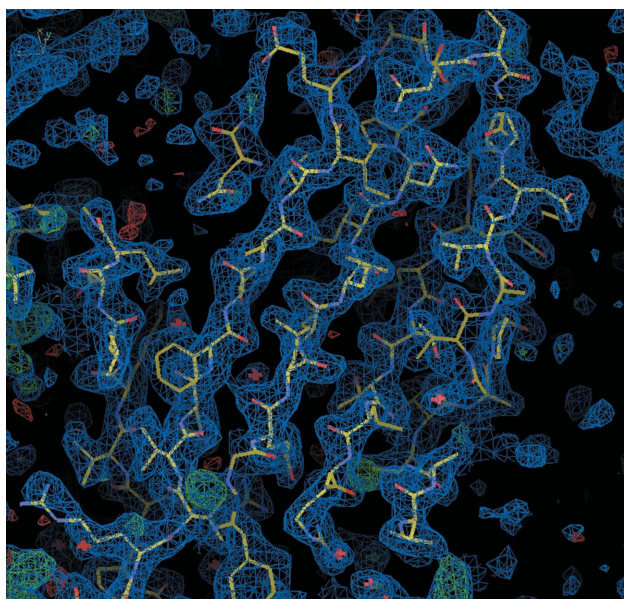
(a)
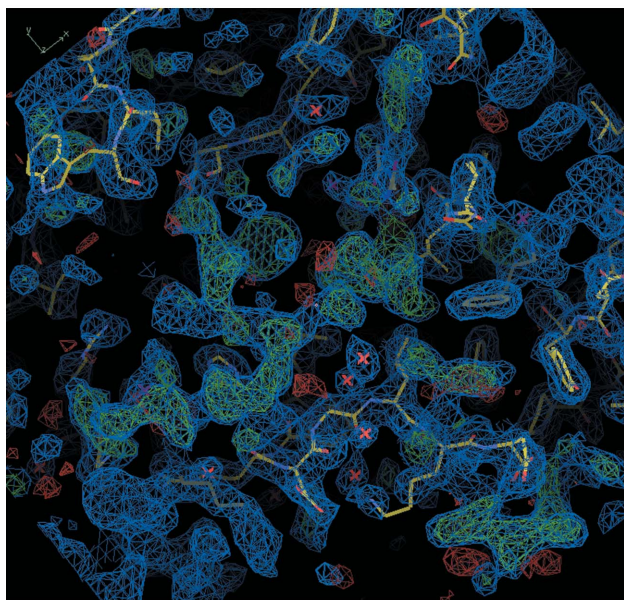
(b)

Figure 1
Electron density maps from *Ac*NiR S-SAD experiments at SOLEIL using λ = 2.07 Å, obtained using *PHENIX* autobuilding routines. (*a*) The 2.2 Å resolution map contoured at 1.0σ (0.35 electrons Å⁻³) for which 61% of the side-chains were automatically fitted into the electron density; (*b*) a region of the map between Val20 and Asp29 where automated model building failed but which is suitable for manual building.

(locating 210 sidechains) in 12 fragments that was suitable for further manual model building (Fig. 1). *ARP/wARP* was not able to build at this resolution but was successful after phase extension to 1.4 Å, generating 316 residues in two main-chain fragments; however, at resolutions below 1.4 Å no more than 7% of the structure was built. Both of these cases represent successful outcomes of the S-phasing experiments with *Ac*NiR.

3.1.2. Experiments at DLS and APS: impact of harmonic contamination. On our first visit to beamline I02 at Diamond,

third-order harmonics from the Si(111) monochromator were found to have a significant intensity at wavelengths longer than 2.1 Å (see Fig. 1 of supplementary material[2]). Harmonic contamination has long been recognized as an almost certain cause for failure of experiments conducted at long wavelengths (Helliwell, 1992; Polentarutti *et al.*, 2004). A control-software improvement implemented on Diamond beamline I03 subsequently enabled the greater part of the harmonic contamination to be suppressed by adjusting the post-monochromator mirrors during beam energy optimization. Successful experiments were then possible using the longest X-ray wavelength (2.4 Å) available on beamline I03. A dataset was collected to 2.69 Å resolution and sub-structure solution and phasing were carried out (Table 2 and Fig. 2) with 314 residues automatically built by *ARP/wARP* using a 'native' dataset extended to a final resolution of 1.3 Å. In addition, using *PHENIX*, it was possible to automatically build 313 residues into the 2.69 Å resolution S-SAD electron density map without the need for a second 'native' high-resolution dataset.

A problem with harmonic contamination of the primary X-ray beam, using wavelengths longer than 1.8 Å, was also encountered during a visit to beamline ID22 at APS.[3] Offsetting the second crystal of the Si(220) monochromator partially reduced the harmonic content,[4] but not sufficiently to allow for a successful data collection for S-phasing purposes at wavelengths longer than 1.9 Å. Attempts at S-SAD phasing were only possible for data obtained from only one (the strongest diffracting) *Ac*NiR crystal of eight measured during these experiments. This was achieved using a dataset measured to 2.24 Å resolution (Table 2). *PHENIX* was subsequently able to solve and build 308 residues in two fragments with this dataset. However, initial sub-structure solution and phasing by the *SHELX* suite and density modification by *DM* did not provide starting phases that were good enough for successful building by *ARP/wARP* (less than 20% of the structure was correctly built in multiple fragments). Phase extension using native data to better than 1.9 Å resolution was required to automatically build 91% of the sequence (309 residues in two fragments) using *ARP/wARP*.

### 3.2. S-SAD phasing with multiple crystals

For many real cases it may be necessary to use multiple isomorphic crystals to obtain the desired data multiplicity for successful S-SAD phasing, for instance when the crystal lifetime in the X-ray beam is limited owing to radiation damage. This situation was simulated by combining diffraction data from three different *Ac*NiR crystals, with approximate dimensions 0.4 × 0.4 × 0.4 mm, 0.15 × 0.15 × 0.15 mm and 0.15 × 0.15 × 0.05 mm. The data were collected using a wavelength of 2.07 Å on beamline 10 at the SRS. For each

---

[2] Supplementary data for this paper are available from the IUCr electronic archives (Reference: WA5024). Services for accessing these data are described at the back of the journal.
[3] To avoid the unwanted harmonics the Si(220) crystal on ID22 has now been replaced by a Si(111) crystal, where the second-order reflection is absent.
[4] The second harmonic is present
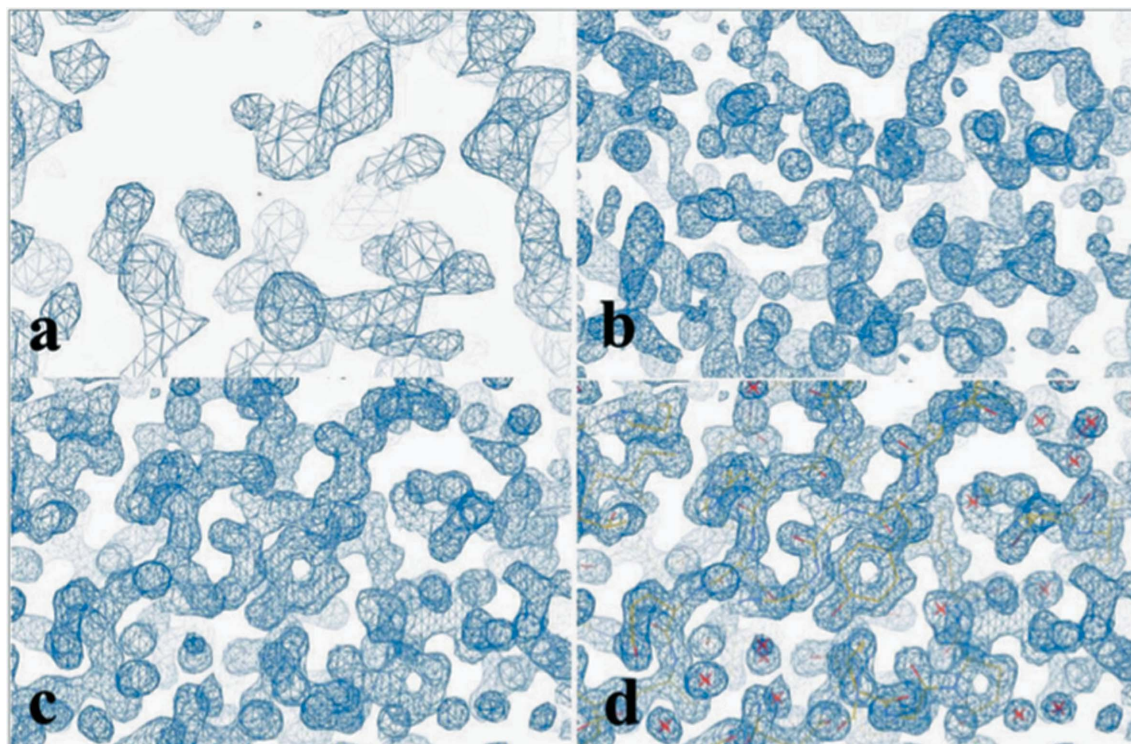
Figure 2
Electron density maps from *Ac*NiR S-SAD experiments at Diamond using λ = 2.4 Å. (*a*) The initial 2.69 Å resolution map contoured at 1.4σ (1.01 electrons Å^{-3}), calculated from *SHELXE* without density modification; (*b*) the map calculated from the experimental phases combined with 'native' amplitudes to 1.3 Å resolution, with density modification contoured at 1.4σ (0.92 electrons Å^{-3}); (*c*) the final electron density map is shown after automated model building using *ARP/wARP*, contoured at 1.4σ (0.75 electrons Å^{-3}); (*d*) the map in (*c*) and the structural model built by *ARP/wARP* are shown together.

crystal a smaller rotation range (120 × 1° oscillation images) was recorded and then data were scaled together (Table 2) to provide a combined dataset with an overall multiplicity of 37. While the scaling statistics are less favourable than in the examples where only one crystal was used, the anomalous differences were accurate enough for the combined scaled dataset to prove suitable for solving using *PHENIX*, with a cut-off resolution of 3 Å being used for the heavy-atom search, and automated model building finding 318 residues in five fragments to a final resolution of 1.96 Å. However, *ARP/wARP* failed with this dataset. The potential advantages of this multi-crystal method for low-resolution phasing have recently been described (Liu *et al.*, 2011).

3.3. Phasing using Cu-SAD at very short wavelengths

Since *Ac*NiR is a copper-containing metalloprotein it should be possible to solve the structure using the anomalous signal from the two Cu atoms per 340 residues. Rather than using SAD (or MAD) optimized for the Cu *K*-edge ($\sim$1.38 Å), we resolved to try a wavelength where the Bijvoet ratio for two Cu atoms was closer to the theoretical Wang limit of 0.6% (Wang, 1985), and significantly smaller than the estimated Bijvoet ratio for the nine S atoms of *Ac*NiR at $\sim$2 Å. In an example shown here (Table 2, Cu-phasing) we obtained excellent sub-structure solutions, phasing and fully automated model building for data measured at the SLS using a wave-

length of 0.75 Å ($f'' = 1.24$) and the Pilatus detector, for an estimated Bijvoet ratio of $\sim$0.75%. We found that a dataset with overall (anomalous) multiplicity as low as 7 (4), but extending to a much higher resolution (1.25 Å) compared with the long-wavelength experiments (Table 2, Fig. 3), was sufficient to be able to solve, phase and automatically build 310 of the 340 residues in two fragments using *ARP/wARP*. In this case the density modification procedure benefited from the higher-resolution data.

3.4. Cu-SAD using sequential datasets at very short wavelength: effect of radiation-induced changes in sub-structures

Fifteen complete low-dose sequential datasets were measured from one crystal at SLS beamline X10SA using the Pilatus-6M detector and an X-ray wavelength of 0.75 Å. The same region of the crystal was exposed to the beam in each dataset, allowing the effects of increasing absorbed X-ray dose on Cu-SAD phasing to be investigated. Each dataset incurred an absorbed X-ray dose of 0.46 MGy resulting in a total dose over 15 datasets of 6.9 MGy. There was a significant degradation in maximum resolution [data limit set at $I/\sigma(I) > 2$ for the outermost resolution shell], from 1.36 Å to 1.69 Å, as shown in Table 3 and Fig. 4, over the 15 datasets, with an approximate linear correlation between accumulated dose and maximum resolution limit. Cu-SAD phasing and automatic model building could be successfully performed using indivi-

Table 3
*SCALA* processing statistics for sequential *Ac*NiR datasets 1, 9 and 15.

Values for the highest-resolution shells are given in parentheses.

	Dataset 1	Dataset 9	Dataset 15
Low-resolution limit (Å)	47.40	47.5	47.54
High-resolution limit (Å)	1.36	1.53	1.69
Accumulated dose† (MGy)	0.46	4.14	6.90
R_{merge} (%)	0.065 (0.785)	0.066 (0.738)	0.073 (0.745)
No. of unique reflections	60994 (8857)	43257 (6227)	31688 (4570)
Mean $[(I)/\sigma(I)]$	14.9 (2.0)	14.4 (2.1)	14.0 (2.1)
Completeness (%)	99.9 (100)	99.9 (100)	99.8 (100)
Multiplicity	5.0 (5.0)	5.0 (5.1)	5.0 (4.8)
Anomalous completeness (%)	95.9 (96.0)	96.1 (97.2)	95.8 (96.1)
Anomalous multiplicity	2.5 (2.4)	2.5 (2.5)	2.5 (2.4)

† Accumulated dose at the end of the dataset, calculated using the program *RADDOSE* (Paithankar *et al.*, 2009).
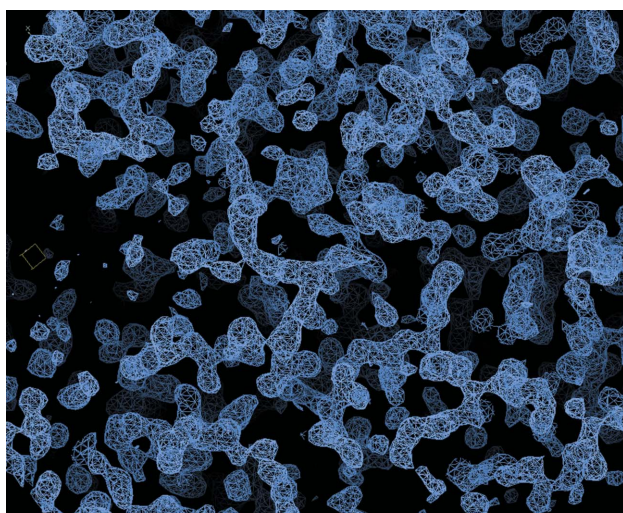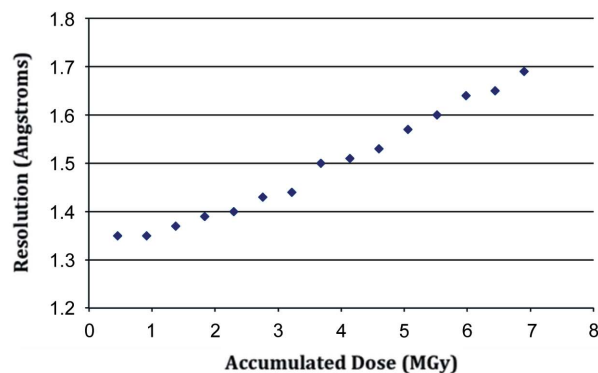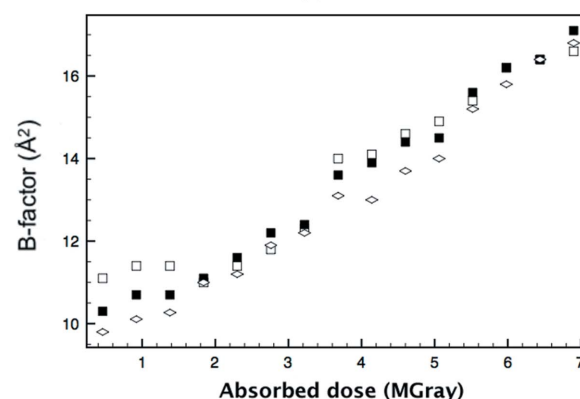

(a)
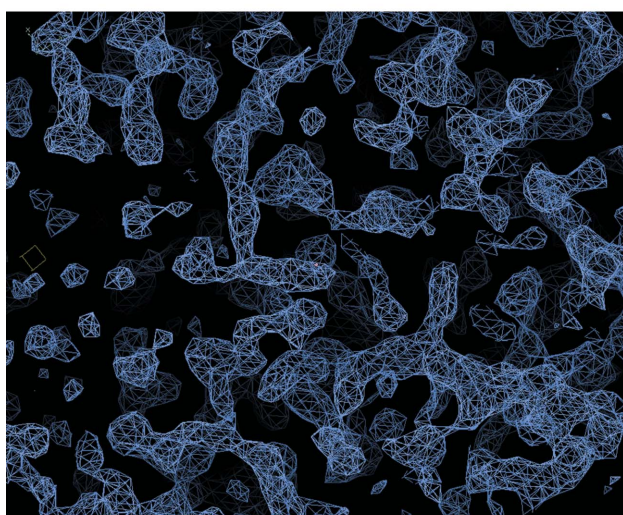
(b)

Figure 3
Electron density from *Ac*NiR Cu-SAD experiments at the SLS using λ = 0.75 Å, calculated from *SHELXE* and following density modification by *DM*. The map covers the same section as in Fig. 1(b) and is shown at (a) 1.25 Å resolution contoured at 1.2σ (0.80 electrons Å^{-3}) and (b) 2.2 Å resolution contoured at 1.1σ (0.69 electrons Å^{-3}).

(a)

(b)

Figure 4
(a) Decrease in maximum resolution as a function of dose for 15 sequential datasets measured from an *Ac*NiR crystal. (b) Refined *B*-factors in the 15 sequential datasets for all atoms (open squares), T1Cu (black squares) and T2Cu (diamonds). Note that the occupancy of the T2Cu atom was 0.8. The ratios of Cu-atom to all-atom *B*-factors were 0.92 (dataset 1) increasing to 1.03 (dataset 15) for T1Cu, with corresponding values for T2Cu of 0.88 and 1.01. In dataset 9, the first for which structure solution and building was not automatically forthcoming, the ratio of Cu-atom to all-atom *B*-factor was 0.99 for T1Cu and 0.92 for the T2Cu. A slight increase in these ratios was thus observed with increasing dose, such that the Cu atoms were less disordered than the average atom in dataset 1 but had above-average *B*-factors by the end of the experiment.

dual datasets 1 to 8, each with a multiplicity of 5 and anomalous multiplicity of 2.5, but failed when using the ninth dataset following an accumulated dose of 4.1 MGy and in all subsequent datasets. In cases where SAD phasing failed, the model generated from dataset 1 was used as the starting model in refinement using *REFMAC5*. A significant difference in SAD phasing power was observed between the first and last dataset, with 301 residues built automatically using *ARP/wARP* for the first dataset, and only 105 residues for dataset 15.

The dose-dependent loss of phasing power can arise either from general radiation damage and increased global disorder and/or from specific damage to the Cu centres. Previous studies have shown that reduction of the T1Cu centre of *Ac*NiR (Antonyuk & Hough, 2011) and *Ax*NiR[5] (Ellis *et al.*, 2008; Hough *et al.*, 2008) by X-rays is relatively rapid, and would be expected to be complete during this experiment,

---

[5] The blue Cu nitrite reductase from *Alcaligenes xylosoxidans*.

typically following a dose of ∼4 MGy (reduction of the T2Cu centre in *Ac*NiR has also been shown to occur albeit slowly and indeed is observed here in the fully refined crystal structure of the 15th dataset). The T1Cu ion would be expected to shift in position by ∼0.1 Å or less as a result of this change of oxidation state (Strange *et al.*, 2005; Antonyuk *et al.*, 2005), a positional shift which could conceivably affect the location of this atom in the 'heavy atom' search and subsequent phasing. Consistent with this view, the shift in Cu position between datasets 1 and 15 was ∼0.08 Å (T1Cu) and 0.03 Å (T2Cu), values that are within the experimental coordinate error (0.11 Å) for dataset 15 and which would normally be considered structurally insignificant. It appears likely that the loss of phasing power from dataset 9 onwards arises from a general deterioration in the data quality rather than to site-specific structural changes.

4. Discussion

We have used *Ac*NiR as a representative model system for S-SAD experiments at long wavelengths, where the Bijvoet values were more than twice the Wang limit, and Cu-SAD experiments at very short wavelengths, where the Bijvoet ratio was significantly smaller and closer to the Wang limit. These data provide an overview of the present capabilities for routinely and automatically solving a structure by these two techniques using non-specialist variable-wavelength synchrotron beamlines. The experiments were performed using an average-sized protein with just below average sulfur content, lacking a di-sulfide bridge, and a below-average solvent content (37%), but with the advantage of being able to grow the crystals in a high-symmetry space group.

Fully automated model building was most successful (*i.e.* building >90% of the model) with *ARP/wARP* when amplitudes from a medium (or high) resolution 'native' dataset (1.9 Å or better) were combined with the low-resolution starting phases from *SHELXE/DM*. *PHENIX* was generally more successful than *ARP/wARP* in building initial models to lower resolutions (>2 Å) using the long-wavelength datasets alone (*i.e.* after density modification using *PHASER* but without phase extension). It is likely that continuing developments in model-building software will extend their capabilities to even lower resolutions. This will be important for working with proteins with a much lower sulfur content than *Ac*NiR, or for more weakly diffracting crystals, where the use of long X-ray wavelengths (>3 Å) will be required to obtain sufficiently strong anomalous data, but at the cost of poorer resolution. Such experiments would require non-standard beamlines with specific design capabilities for working with long wavelengths, such as those currently being planned or constructed for phase III at Diamond and at APS, ESRF and the Photon Factory.

Data multiplicity and a high signal-to-noise ratio are key parameters for long-wavelength phasing experiments (Cianci *et al.*, 2008; Dauter & Adamiak, 2001; Ramagopal *et al.*, 2003; Sarma & Karplus, 2006; Weiss, Sicker, Djinovic Carugo *et al.*, 2001), while suppression or rejection of higher harmonic contamination of the primary X-ray beam is an essential precondition for success, as is the absence or minimization of radiation damage. No clear wavelength dependence for the anomalous signal-to-noise ratio emerges from the different datasets, and the present set of experiments for *Ac*NiR (Table 2) showed that a multiplicity of ∼40 (with anomalous multiplicity ∼20) was suitable for successful S-SAD structure solution and automated model building, essentially independent of the wavelength (1.9 to 2.4 Å) or beamline/source used. The estimated I/σ(asymptoptic) values were in the range 15–16 for long-wavelength experiments and 15–22 for Cu-phasing experiments, suggesting a degree of equivalence for the instrumental performance of the different beamlines used (Diederichs, 2010). The beamlines were equally capable of producing a successful S-SAD solution for experiments on the *Ac*NiR crystals.

The intrinsic crystalline order and scattering power of the S sites in the crystals may be a limiting factor in reducing the minimum data multiplicity, and substantially longer X-ray wavelengths than those used here (with correspondingly stronger anomalous scattering) may be required to significantly reduce the required multiplicity (by increasing the accuracy of the anomalous data obtained). The long-wavelength beamlines currently being planned would provide advantages over standard wavelength tunable beamlines for this purpose.

Consideration should also be given to the use of detector arrangements that make full use of all the available reflections from a given crystal, extending the resolution limit at a particular X-ray wavelength as far as possible for phasing and model-building purposes, for example through the use of a 2θ scanning arm (Cianci *et al.*, 2008) or by employing larger area detectors such as Pilatus-6M (Hülsen *et al.*, 2006) or MAR flat panel, provided a sufficiently high completeness can be achieved. However, the type of detector used was not a significant factor in the outcome of the experiments presented here, but for protein crystals, that may be more dose-sensitive than *Ac*NiR, the rapid data collection afforded by the Pilatus detector should be an advantage for collecting the required high-multiplicity datasets for a given radiation dose.

The high symmetry of the *Ac*NiR crystals in the present case helped in minimizing the X-ray dose received by the crystals. While there was no apparent decline in diffraction during measurement of the high-redundancy long-wavelength datasets, the $R_{\mathrm{anom}}/R_{\mathrm{p.i.m.}}$ ratios for the first and last 360° of data indicated (*e.g.* Table 2, DLS/I03) that a decline in the anomalous signal generally occurred over time owing to the accumulated X-ray dose. The experiments provided data of sufficient quality and accuracy to be able to go from diffraction images to the final model in a routine automated fashion using the standard software packages in ∼60% of the crystals measured.

$R_{\mathrm{anom}}/R_{\mathrm{p.i.m.}}$, like other anomalous data quality indicators (Wang *et al.*, 2006), ought to become more reliable with increased multiplicity but its magnitude does not provide a guarantee that phasing with a particular dataset will succeed (Dauter, 2006), only that it may be worthwhile making an

attempt at structure solution. Therefore, at the beamline and during the experiments it was only possible to scale the S-SAD datasets to different degrees of multiplicity and estimate the anomalous signal, for example using the d''/σ values from *SHELXC* (Table 2), and undertake quick trials of *SHELXD* for indications of success. Generally, however, the main effort in structure solution, phasing and model building was accomplished away from the beamline. While there are many excellent automated structure solution pipelines available at beamlines around the world, this is still likely to be the case for 'non-expert' users of S-SAD phasing methods. In more difficult cases, for example crystals in lower-symmetry space groups or with weaker anomalous scattering, the likelihood of users leaving the beamline knowing that the experiment was a success (*i.e.* that a structure will emerge) is doubtful. One of the reasons for collecting 720° datasets in our own experiments was the uncertainty associated with our initial attempts to solve the structures at the beamline using lower-multiplicity (360°) datasets. For a typical Se-Met experiment, whether SAD or MAD, the success or otherwise of the experiment is more certainly known while users are at the beamline and can take appropriate action. The situation for S-SAD experiments during data collection could be further improved if there were more reliable and rapid indicators of anomalous data quality for predicting success.

It is common to perform anomalous MAD/SAD experiments on metalloprotein crystals by collecting data optimized for f'' or f' at specific wavelengths that are close to an X-ray absorption edge, limiting the resolution of the data even for well diffracting crystals. By using the shortest wavelength at which a sufficient anomalous signal can be measured from a metalloprotein, a SAD dataset can readily be obtained from suitably diffracting crystals at or near atomic resolution if desired. The present example of Cu-SAD phasing at very short wavelengths has clearly demonstrated what can be accomplished by automated structure solution, where phasing from relatively low multiplicity datasets (multiplicity as low as 5 with anomalous multiplicity of only 2.5, Table 2) benefits from the increased scattering power of the metal atom substructure relative to that of sulfur. The automated structure solution and model building extends in such cases to high resolutions, which is advantageous for density modification using *SHELXE*. Structure determination was readily achieved in most cases with just a few cycles of *ARP/wARP* needed to build more than 90% of the structure. The lower than average temperature factors of the Cu atoms in *Ac*NiR means that their anomalous contribution also extends above the background noise to relatively higher resolutions. Interestingly, Cu-phasing was successful despite the d''/σ estimates from *SHELXC* indicating only a poor anomalous signal (Table 2). This approach may apply in general for proteins containing intrinsic metal atoms. For well diffracting crystals the shortest wavelength that provides a measurable (or estimated) anomalous signal is suitable for such experiments, while for collecting weaker diffraction data a compromise between the shortest and optimum wavelengths could be selected. For *Ac*NiR, a progressive lowering of the resolution limit and loss

of phasing power resulted from the accumulation of X-ray dose until, at a dose of 4.1 MGy, it was no longer possible to automatically solve and build the structure. The datasets with lower accumulated dose measured before this point (having less radiation damage) were each amenable to the automated methods indicating that in this case phasing could be achieved using around 11% of the dose which would prevent structure solution.

Lower data multiplicity was required for successful Cu-phasing at short wavelengths compared with S-phasing at long wavelengths. While this is in part due to the relatively lower than protein-average B-factors for the Cu atoms compared with S atoms in *Ac*NiR, the observation that the 0.75 Å X-ray Cu anomalous data required a factor of five less multiplicity compared with the S anomalous data points to a number of current experimental limitations for S-SAD. Thus, in principle, concerted efforts to improve the long-wavelength (2 to 2.4 Å) data quality could provide high dividends and suggests that lower data multiplicity than is currently required should in general be possible for sulfur phasing. For a protein with average or lower sulfur content, S-SAD is not yet a routine method, comparable with Se-Met, for automated structure solution using existing synchrotron beamlines and using current software tools. The accuracy of long-wavelength datasets remains limited by a number of factors including purity of X-ray beams, non-optimized source/monochromator/mirror combinations, the size, geometry and quantum efficiency of detectors, the higher X-ray absorption by crystals, beamline airpaths and detector-windows and the increased radiation damage. Suggestions for improving existing standard synchrotron beamlines for phasing at long wavelengths have included incorporating helium beam paths to improve background and minimize air-absorption losses in the primary and secondary beams (Polentarutti *et al.*, 2004). The use of X-ray tomography to obtain accurate crystal sizes to improve absorption corrections at long wavelengths has also been suggested (Brockhauser *et al.*, 2008) and is being implemented at some beamlines, such as the phase III beamline I23 at DLS due to become operational in 2013. In cases where radiation damage is a major concern, careful consideration of the absorption properties of components of the mother liquor/cryoprotectants, reducing background by removing or minimizing the amount of cryoprotectant used (Kitago *et al.*, 2005, 2010; Kim *et al.*, 2007) or indeed the use of radical scavengers (De la Mora *et al.*, 2011) may help in producing a successful outcome.

Experiments need to be better informed on the effect of X-ray dose on changes in relevant sub-structures with dose and their effect in phasing power. In some cases the use of on-line spectroscopic monitoring during X-ray crystallography experiments may be highly beneficial. The long-wavelength beamlines and upgrades currently being proposed or under construction at Diamond, APS, ESRF and the Photon Factory could be further enhanced by incorporating such facilities by design rather than retro-fitting to what is normally a crowded environment (Hough *et al.*, 2008; Owen *et al.*, 2009; Stoner-Ma *et al.*, 2011; Orville *et al.*, 2011). A strategy of 'maximum data

for minimum dose' with minimum changes in phasing substructure can then be implemented in a user-friendly manner.

5. Conclusion

We have shown that much lower redundancy data than is currently used for S-SAD phasing can yield a structure solution for weak anomalous scattering units close to the Wang limit. We are persuaded that concerted efforts that improve the quality of data measured at long wavelengths (2 to 2.4 Å) could provide high dividends for sulfur phasing. S-SAD can thus become a routine method of phase determination for proteins with an average sulfur content.

References

Adams, P. D., Afonine, P. V., Bunkóczi, G., Chen, V. B., Davis, I. W., Echols, N., Headd, J. J., Hung, L.-W., Kapral, G. J., Grosse-Kunstleve, R. W., McCoy, A. J., Moriarty, N. W., Oeffner, R., Read, R. J., Richardson, D. C., Richardson, J. S., Terwilliger, T. C. & Zwart, P. H. (2010). *Acta Cryst.* D**66**, 213–221.
Adams, P. D., Grosse-Kunstleve, R. W., Hung, L.-W., Ioerger, T. R., McCoy, A. J., Moriarty, N. W., Read, R. J., Sacchettini, J. C., Sauter, N. K. & Terwilliger, T. C. (2002). *Acta Cryst.* D**58**, 1948–1954.
Alkire, R. W., Duke, N. E. C. & Rotella, F. J. (2008). *J. Appl. Cryst.* **41**, 1122–1133.
Antonyuk, S. V. & Hough, M. A. (2011). *Biochim. Biophys. Acta*, **1814**, 778–784.
Antonyuk, S. V., Strange, R. W., Sawers, G., Eady, R. R. & Hasnain, S. S. (2005). *Proc. Natl Acad. Sci.* **102**, 12041–12046.
Behrens, W., Otto, H., Stuhrmann, H. B. & Heyn, M. P. (1998). *Biophys. J.* **75**, 255–263.
Boesecke, P., Bois, J. M., Crépin, T., Hunte, C., Kahn, R., Kao, W.-C., Nauton, L., Winther, A.-M. L., Moller, J., Nissen, P., Nury, H., Olesen, C., Pebay-Peyroula, E., Vicat, J. & Stuhrmann, H. (2009). *J. Synchrotron Rad.* **16**, 658–665.
Brockhauser, S., Di Michiel, M., McGeehan, J. E., McCarthy, A. A. & Ravelli, R. B. G. (2008). *J. Appl. Cryst.* **41**, 1057–1066.
Carpentier, P., Boesecke, P., Bois, J.-M., Chesne, M.-L., Fanchon, E., Kahn, R., Stuhrmann, H. & Vicat, J. (2002). *Acta Phys. Pol.* **101**, 603–612.
Cianci, M., Helliwell, J. R. & Suzuki, A. (2008). *Acta Cryst.* D**64**, 1196–1209.
Collaborative Computational Project, Number 4 (1994). *Acta Cryst.* D**50**, 760–763.
Cowtan, K. (1994). *Jnt CCP4/ESF-EAMCB Newsl. Protein Crystallogr.* **31**, 34–38.

Dauter, Z. (2006). *Acta Cryst.* D**62**, 867–876.
Dauter, Z. & Adamiak, D. A. (2001). *Acta Cryst.* D**57**, 990–995.
Dauter, Z., Dauter, M., de La Fortelle, E., Bricogne, G. & Sheldrick, G. M. (1999). *J. Mol. Biol.* **289**, 83–92.
Debreczeni, J. É., Bunkóczi, G., Ma, Q., Blaser, H. & Sheldrick, G. M. (2003). *Acta Cryst.* D**59**, 688–696.
De la Mora, E., Carmichael, I. & Garman, E. F. (2011). *J. Synchrotron Rad.* **18**, 346–357.
Diederichs, K. (2010). *Acta Cryst.* D**66**, 733–740.
Djinović Carugo, K., Helliwell, J. R., Stuhrmann, H. & Weiss, M. S. (2005). *J. Synchrotron Rad.* **12**, 410–419.
Ellis, M. J., Buffey, S. G., Hough, M. A. & Hasnain, S. S. (2008). *J. Synchrotron Rad.* **15**, 433–439.
Emsley, P. & Cowtan, K. (2004). *Acta Cryst.* D**60**, 2126–2132.
Evans, P. (2006). *Acta Cryst.* D**62**, 72–82.
González, A., von Delft, F., Liddington, R. C. & Bakolitsa, C. (2005). *J. Synchrotron Rad.* **12**, 285–291.
Grosse-Kunstleve, R. W. & Adams, P. D. (2003). *Acta Cryst.* D**59**, 1966–1973.
Heinrich, B., Bergamaschi, A., Broennimann, C., Dinapoli, R., Eikenberry, E. F., Johnson, I., Kobas, M., Kraft, P., Mozzanica, A. & Schmitt, B. (2009). *Nucl. Instrum. Methods Phys. Res. A*, **607**, 247–249.
Helliwell, J. R. (1992). *Macromolecular Crystallography with Synchrotron Radiation.* Cambridge University Press.
Hendrickson, W. A. & Teeter, M. M. (1981). *Nature (London)*, **290**, 107–113.
Hough, M. A., Antonyuk, S. V., Strange, R. W., Eady, R. R. & Hasnain, S. S. (2008). *J. Mol. Biol.* **378**, 353–361.
Hülsen, G., Broennimann, C., Eikenberry, E. F. & Wagner, A. (2006). *J. Appl. Cryst.* **39**, 550–557.
Kabsch, W. (2010). *Acta Cryst.* D**66**, 125–132.
Kim, C. U., Hao, Q. & Gruner, S. M. (2007). *Acta Cryst.* D**63**, 653–659.
Kitago, Y., Watanabe, N. & Tanaka, I. (2005). *Acta Cryst.* D**61**, 1013–1021.
Kitago, Y., Watanabe, N. & Tanaka, I. (2010). *J. Appl. Cryst.* **43**, 341–346.
Langer, G., Cohen, S. X., Lamzin, V. S. & Perrakis, A. (2008). *Nat. Protoc.* **3**, 1171–1179.
Lemke, C. T., Smith, G. D. & Howell, P. L. (2002). *Acta Cryst.* D**58**, 2096–2101.
Leslie, A. G. W. (1992). *Jnt CCP4/ESF-EAMCB Newsl. Protein Crystallogr.* **26**, 27–33.
Liu, Q., Zhang, Z. & Hendrickson, W. A. (2011). *Acta Cryst.* D**67**, 45–59.
Liu, Z. J., Vysotski, E. S., Chen, C. J., Rose, J. P., Lee, J. & Wang, B. C. (2000). *Protein Sci.* **9**, 2085–2093.
McCoy, A. J., Grosse-Kunstleve, R. W., Adams, P. D., Winn, M. D., Storoni, L. C. & Read, R. J. (2007). *J. Appl. Cryst.* **40**, 658–674.
Mooij, W. T., Cohen, S. X., Joosten, K., Murshudov, G. N. & Perrakis, A. (2009). *Structure*, **17**, 183–189.
Morris, R. J., Perrakis, A. & Lamzin, V. S. (2003). *Methods Enzymol.* **374**, 229–244.
Mueller-Dieckmann, C., Panjikar, S., Schmidt, A., Mueller, S., Kuper, J., Geerlof, A., Wilmanns, M., Singh, R. K., Tucker, P. A. & Weiss, M. S. (2007). *Acta Cryst.* D**63**, 366–380.
Mueller-Dieckmann, C., Panjikar, S., Tucker, P. A. & Weiss, M. S. (2005). *Acta Cryst.* D**61**, 1263–1272.
Murshudov, G. N., Vagin, A. A. & Dodson, E. J. (1997). *Acta Cryst.* D**53**, 240–255.
Nan, J., Zhou, Y., Yang, C., Brostromer, E., Kristensen, O. & Su, X.-D. (2009). *Acta Cryst.* D**65**, 440–448.
Orville, A. M., Buono, R., Cowan, M., Héroux, A., Shea-McCarthy, G., Schneider, D. K., Skinner, J. M., Skinner, M. J., Stoner-Ma, D. & Sweet, R. M. (2011). *J. Synchrotron Rad.* **18**, 358–366.

Otwinowski, Z. & Minor, W. (1997). *Macromolecular Crystallography*, Part A, edited by C. W. Carter and R. M. Sweet, pp. 307–326. New York: Academic Press.

Owen, R. L., Pearson, A. R., Meents, A., Boehler, P., Thominet, V. & Schulze-Briese, C. (2009). *J. Synchrotron Rad.* **16**, 173–182.

Paithankar, K. S., Owen, R. L. & Garman, E. F. (2009). *J. Synchrotron Rad.* **16**, 152–162.

Perrakis, A., Morris, R. & Lamzin, V. S. (1999). *Nat. Struct. Biol.* **6**, 458–463.

Polentarutti, M., Glazer, R. & Djinović Carugo, K. (2004). *J. Appl. Cryst.* **37**, 319–324.

Ramagopal, U. A., Dauter, M. & Dauter, Z. (2003). *Acta Cryst.* D**59**, 1020–1027.

Ravelli, R. B. & Garman, E. F. (2006). *Curr. Opin. Struct. Biol.* **16**, 624–629.

Ravelli, R. B. G., Nanao, M. H., Lovering, A., White, S. & McSweeney, S. (2005). *J. Synchrotron Rad.* **12**, 276–284.

Sarma, G. N. & Karplus, P. A. (2006). *Acta Cryst.* D**62**, 707–716.

Schneider, T. R. & Sheldrick, G. M. (2002). *Acta Cryst.* D**58**, 1772–1779.

Sheldrick, G. M. (2002). *Z. Kristallogr.* **217**, 644–650.

Sheldrick, G. M. (2008). *Acta Cryst.* A**64**, 112–122.

Stoner-Ma, D., Skinner, J. M., Schneider, D. K., Cowan, M., Sweet, R. M. & Orville, A. M. (2011). *J. Synchrotron Rad.* **18**, 37–40.

Strange, R. W., Ellis, M. J. & Hasnain, S. S. (2005). *Coord. Chem. Rev.* **249**, 197–208.

Stuhrmann, S., Bartels, K. S., Braunwarth, W., Doose, R., Dauvergne, F., Gabriel, A., Knöchel, A., Marmotti, M., Stuhrmann, H. B., Trame, C. & Lehmann, M. S. (1997). *J. Synchrotron Rad.* **4**, 298–310.

Terwilliger, T. (2004). *J. Synchrotron Rad.* **11**, 49–52.

Terwilliger, T. C., Grosse-Kunstleve, R. W., Afonine, P. V., Moriarty, N. W., Zwart, P. H., Hung, L.-W., Read, R. J. & Adams, P. D. (2008). *Acta Cryst.* D**64**, 61–69.

Usón, I., Stevenson, C. E. M., Lawson, D. M. & Sheldrick, G. M. (2007). *Acta Cryst.* D**63**, 1069–1074.

Wang, B. C. (1985). *Diffraction Methods for Biological Macromolecules*, pp. 90–112. New York: Academic Press.

Wang, J., Dauter, M. & Dauter, Z. (2006). *Acta Cryst.* D**62**, 1475–1483.

Watanabe, N., Kitago, Y., Tanaka, I., Wang, J., Gu, Y., Zheng, C. & Fan, H. (2005). *Acta Cryst.* D**61**, 1533–1540.

Weiss, M. S. (2001). *J. Appl. Cryst.* **34**, 130–135.

Weiss, M. S., Sicker, T., Djinovic-Carugo, K. & Hilgenfeld, R. (2001). *Acta Cryst.* D**57**, 689–695.

Weiss, M. S., Sicker, T. & Hilgenfeld, R. (2001). *Structure*, **9**, 771–777.

Yang, C., Pflugrath, J. W., Courville, D. A., Stence, C. N. & Ferrara, J. D. (2003). *Acta Cryst.* D**59**, 1943–1957.